Optogenetic dissection of the roles of actomyosin in the mechanics underlying tissue fluidity

R. Marisol Herrera-Perez, Christian Cupo, Cole Allan, Alicia B. Dagle, Karen E. Kasza

Department of Mechanical Engineering, Columbia University, New York, New York, 10027, USA
Corresponding author: Karen E. Kasza, karen.kasza@columbia.edu

ABSTRACT

Rapid epithelial tissue flows are essential to building and shaping developing embryos. However, it is not well understood how the mechanical properties of tissues and the forces driving them to flow are jointly regulated to accommodate rapid tissue remodeling. To dissect the roles of actomyosin in the mechanics of epithelial tissue flows, here we use two optogenetic tools, optoGEF and optoGAP, to manipulate Rho/Rho-kinase signaling and actomyosin contractility in the germband epithelium, which flows via convergent extension during *Drosophila* body axis elongation. The ability to perturb actomyosin across the tissue allows us to analyze the effects of actomyosin on cell rearrangements, tissue tensions, and tissue mechanical properties. We find that *either* optogenetic activation or deactivation of Rho1 signaling and actomyosin contractility at the apical surface of the germband disrupts cell rearrangements and tissue-level flows. By probing mechanical tensions in the tissue using laser ablation and predicting tissue mechanical properties from cell packings, we find that actomyosin influences *both* the anisotropic forces driving tissue flow and the mechanical properties of the tissue resisting flow, leading to complex relationships between actomyosin activity and tissue-level flow. Moreover, our results indicate that changes in the distribution of medial and junctional myosin in the different perturbations alter tissue tension and cell packings in distinct ways, revealing how junctional and medial myosin have differential roles in promoting and orienting cell rearrangements to tune tissue flows in developing embryos.

INTRODUCTION

Within developing embryos, epithelial tissue sheets can dramatically deform to help lay out and shape the basic body plan of the animal. Many epithelial tissue movements are rapid and involve significant remodeling of the tissue through local cell rearrangements that alter the relative positions of cells within the tissue, similar to the deformation and flow of fluid materials (1–3). Based on this similarity to fluid-like material deformation, the ability of a tissue to flow via cell rearrangements is often referred to as *tissue fluidity*. To understand the origins of these tissue-scale flows, we must understand both the mechanical forces that drive the flow and the mechanical properties of the tissue that determine how the tissue resists flowing in response to these forces. Recent studies suggest that the mechanical properties of tissues within developing embryos are regulated in space and time to allow (or prevent) rapid tissue remodeling and flow (4–8). However, the molecular and cellular mechanisms involved in this regulation remain unclear.

Contractile networks of F-actin and non-muscle myosin II, jointly referred to as *actomyosin*, are a primary force-generating machinery in epithelial cells, with specific patterns of myosin localization and contractile activity correlating with tissue-level flow patterns (1, 9–11). In addition, the mechanical behavior of the actomyosin cytoskeleton within cells has been implicated in controlling

the mechanical properties of cells and the tissues in which they reside, with increased actomyosin-generated tension typically associated with stiffer cells and more solid-like tissues (12), which would be predicted to increase resistance to flow. Given these potential dual roles for actomyosin in regulating both tissue-scale driving forces and tissue mechanical properties, it is not well understood how patterns of actomyosin contractility might be regulated to tune tissue fluidity and overall tissue flow.

Body axis elongation in the *Drosophila* embryo is a powerful model system for studying the molecular and cellular mechanisms that contribute to epithelial tissue flows. During this morphogenetic event, the germband epithelium rapidly extends along the head-to-tail (anterior-posterior) body axis and narrows along the dorsal-ventral axis, a process driven by both cell rearrangements (13–17) and changes in cell shape (16, 18–20). Planar polarized patterns of myosin II localization and activity are required for convergent extension of the germband tissue (14, 15, 21–26). The planar polarized myosin pattern generates anisotropic forces in the tissue that are thought to drive and orient cell rearrangement and directional tissue flow. Recent work from our group and others has demonstrated that the onset of rapid cell rearrangements in the germband is predicted by a solid-to-fluid transition in anisotropic vertex models of epithelial tissues (4), suggesting that the mechanical properties of the germband might be regulated to promote this rapid change in tissue shape. However, it is unclear what role actomyosin might play in regulating this change in germband mechanical properties.

Here, we dissect the roles of actomyosin in tissue flows during *Drosophila* body axis elongation. This requires precise perturbation of actomyosin contractility patterns, specifically in the germband during body axis elongation, so that the mechanical behavior of neighboring regions of the embryo is not disturbed. Because this is not possible with traditional molecular genetics approaches, here we employed two optogenetic tools, optoGEF and optoGAP, to manipulate the localization of upstream regulators of *Drosophila* Rho1 at the apical surface of the germband epithelium (27). These tools are based on the CRY2/CIB1 heterodimerization system, which can be activated by blue-light illumination (28–31). The optoGEF tool is based on the full-length *Drosophila* RhoGEF2 protein and activates actomyosin contractility (27). In contrast, optoGAP is based on the full-length *Drosophila* RhoGAP71E protein and deactivates actomyosin contractility (27). Photoactivation via blue light illumination of the apical surface of the germband leads to rapid accumulation of the CRY2 component of the optogenetic tools at the apical cell membrane, allowing us to perturb actomyosin contractility rapidly at minute timescales and specifically in the germband tissue during body axis elongation (27). Employing this optogenetics approach, we analyzed how perturbing actomyosin affects cell rearrangements (a measure of tissue fluidity) using live imaging and quantitative image analysis, how it affects mechanical forces in the tissue using laser ablation experiments, and how it affects mechanical properties of the tissue by analyzing the structure of epithelial cell packings. Our findings indicate that actomyosin influences both the driving forces and tissue mechanical properties and reveal how distinct aspects of the actomyosin machinery in cells promote cell rearrangement and tissue flow.

RESULTS AND DISCUSSION

Optogenetic manipulation of Rho signaling disrupts cell rearrangements and tissue flow during convergent extension

To test how Rho1 signaling and actomyosin contractility influence tissue fluidity during convergent extension, we used light-gated optoGEF and optoGAP tools to manipulate Rho1/Rho-kinase signaling in the germband epithelium of the *Drosophila* embryo during body axis elongation (Fig 1*A,B*) and analyzed the effects on cell rearrangements and tissue flow. We generated embryos

expressing the optoGEF or optoGAP tool using the Gal4/UAS system and illuminated the apical surface of the ventrolateral region of the germband epithelium with blue light (488 nm), beginning at the onset of body axis elongation, which we define as $t = 0$. We captured time-lapse confocal movies and used quantitative image analysis to quantify the effects on the number of cell rearrangements and overall tissue elongation.

First, we analyzed the effects of optogenetic perturbation of Rho1 signaling on the number of cell rearrangements that occur in the tissue, a metric for *tissue fluidity*, i.e. the ability of a tissue to remodel and flow. In control embryos expressing only the CIBN-pmGFP component of the optogenetic system, there were 1.25 ± 0.19 cell rearrangements initiated per cell in the germband during the first 15 min of axis elongation, similar to that seen in wild-type embryos (17, 25, 32, 33) (Fig 1*C*). In contrast, under blue-light illumination of the ventrolateral region of the germband, there were 0.93 ± 0.05 rearrangements per cell in optoGEF embryos ($P = 0.04$ compared to controls), and 0.40 ± 0.12 rearrangements per cell in optoGAP embryos ($P = 0.03$ compared to controls) (Fig 1*C*). Consistent with reduced cell rearrangements, which involve transient cell configurations in which four or more cells meet at a common vertex, activated optoGEF and optoGAP embryos displayed a decrease in average vertex coordination number in the germband (3.07± 0.04, $P = 0.05$ for optoGEF and 3.07± 0.02, $P = 0.04$ for optoGAP at $t = 15$ min) compared to control embryos (3.18 ± 0.01 at $t = 15$ min) (Fig. 1*E*). Taken together, these results show that cell rearrangements are reduced when Rho1 activity is *either* increased (optoGEF) or decreased (optoGAP) in the germband, although the defects are more severe when Rho1 activity is decreased. This is consistent with key roles for Rho1 signaling and actomyosin contractility in controlling tissue fluidity.

Next, we analyzed how these changes in tissue fluidity influence macroscopic tissue flow. In control embryos expressing only the CIBN-pmGFP component of the optogenetic system, the germband tissue elongated 1.71 ± 0.09-fold along the head-to-tail axis (Fig. 1*F*, $t = 15$ min), similar to in wild-type embryos (4, 16, 17, 25, 32). In contrast, the germband in optoGEF embryos elongated 1.37 ± 0.09-fold ($P = 0.06$), while the germband in optoGAP embryos elongated 1.29 ± 0.05-fold ($P = 0.02$) (Fig. 1*F*), consistent with the notion that cell rearrangements mediate tissue flow during convergent extension. Interestingly, tissue-level elongation was similar in both the optoGEF and optoGAP perturbations, despite there being more rearrangements initiated in optoGEF compared to optoGAP embryos, suggesting that other factors might be differentially altered by these perturbations, such as cell shape or the spatial orientation of cell rearrangements.

To take a closer look at cell rearrangements and tissue flow, and the relationships between them, we analyzed the instantaneous rates of cell rearrangement and tissue elongation. In control embryos, the rate of relative tissue elongation increases during the first 10 min of axis elongation to a value of 0.05 ± 0.01 min^{-1} at $t = 10$ min, followed by a decrease during the rest of the process (Fig. 1*D,G*). The cell rearrangement rate follows a similar trend, reaching a value of 0.12 ± 0.04 $cell^{-1}$ min^{-1} at $t = 10$ min, but with a delay relative to tissue elongation (Fig. 1*G*). This delay is possibly associated with cell shape changes during this time that can contribute to tissue-level elongation (16, 18, 20). In optoGEF and optoGAP embryos, the rates of relative tissue elongation and cell rearrangement were both decreased (Fig. 1*H,I*). At $t = 10$ min, the rate of tissue elongation was reduced to 0.02 ± 0.01 min^{-1} in optoGEF ($P = 0.09$) and 0.02 ± 0.06 min^{-1} in optoGAP embryos ($P = 0.03$). At $t = 10$ min, the rate of cell rearrangements was 0.08 ± 0.03 $cell^{-1}$ min^{-1} in optoGEF ($P = 0.45$) and 0.04 ± 0.02 $cell^{-1}$ min^{-1} in optoGAP embryos ($P = 0.09$). The instantaneous rates of tissue elongation and the rates of cell rearrangement are correlated in all embryo groups (Fig. 1*J*, correlation coefficient for control=0.93, optoGEF=0.58, optoGAP=0.71), consistent with a central role for tissue fluidity in promoting tissue elongation. Notably, however, the rate of cell rearrangement was the least predictive of tissue elongation rate for the optoGEF perturbation.

Taken together, these results demonstrate that optogenetic perturbation of Rho1 signaling and actomyosin activity at the apical surface of the germband epithelium disrupts cell rearrangements, decreasing the ability of the tissue to remodel and flow like a fluid during convergent extension.

Patterns of Rho signaling influence predicted tissue mechanical properties, which characterize resistance to tissue flow

To understand why a tissue accommodates (or resists) rapid remodeling and flow, one must consider both the mechanical forces that act on the tissue to drive flow and the tissue mechanical properties that capture how the tissue resists flowing under those forces. Planar polarized patterns of actomyosin in the germband generate contractile forces that are thought to be driving forces for tissue flow (14, 15, 21–23, 25, 26). In addition, actomyosin contractility has also been proposed to influence the mechanical properties of epithelial tissues, with increased actomyosin-generated tension predicted to increase the resistance of the tissue to flow (12). Because actomyosin potentially plays dual roles in influencing how tissues flow, we wondered if effects on driving forces and/or tissue mechanical properties could explain the observed reductions in tissue fluidity when Rho activity is perturbed.

First, we tested if tissue mechanical properties are altered when the elongating germband is photoactivated in optoGEF or optoGAP embryos. Because direct mechanical measurements to probe the mechanical response of the germband remain a significant experimental challenge, we gained insight from predictions of anisotropic vertex models of epithelial tissues. Recent work from our group and others has demonstrated that the fluid-like versus solid-like behavior of epithelia can be predicted from analysis of cell packings in the tissue, which can be extracted from images of cell outlines (4, 6, 34, 35). In particular, for anisotropic tissues like the germband (Fig. 2*A*), two metrics of cell packings in a tissue, the average cell shape index $\bar{p}$ and cell shape alignment index *Q*, are sufficient to classify a given packing as either solid-like or fluid-like (4) (Fig. 2*B*). To gain insight into how Rho signaling influences germband tissue mechanical properties, we analyzed cell shape and alignment in photoactivated control, optoGEF, and optoGAP embryos.

We quantified how the average cell shape index, $\bar{p}$ (cell perimeter divided by the square root of cell area, averaged across the cells in the tissue), and the cell shape alignment index, *Q* (average cell elongation across the tissue, similar to a nematic order parameter but modulated by the extent of cell elongation), in the germband varied over time following blue-light illumination of the ventrolateral region of the germband beginning at the onset of axis elongation. In control embryos expressing only the CIBN-pmGFP component of the optogenetic system, the average cell shape index, $\bar{p}$, increased over time and the cell shape alignment index, *Q*, showed a peak around $t = 2$ min (Fig. 2*A*,*C,D*), similar to in wild-type embryos (4). Comparing these results to the predictions of the anisotropic vertex model (4) suggests that the germband tissue in control embryos starts out near the predicted solid-fluid transition line in *p*-*Q* parameter space and over time moves deeper into the predicted fluid-like region during tissue elongation (Fig. 2*F*), consistent with tissue properties becoming more fluid-like to minimize resistance to flow during axis elongation.

In contrast, cell packings in the germband of photoactivated optoGEF and optoGAP embryos were altered in distinct ways, leading to differences in predicted tissue mechanical properties. In photoactivated optoGAP embryos, the average cell shape index $\bar{p}$ was increased compared to controls during the first 10 min of the process, and the alignment index *Q* showed similar trends as controls with somewhat elevated values of alignment compared to controls throughout the process (Fig. 2*A,C,D*). Comparing these results to the vertex model predictions suggests that in

optoGAP embryos, the germband starts out near the predicted solid-fluid transition line, similar to controls, but does not move as deeply into the predicted fluid-like region (Fig. 2*H*), possibly consistent with somewhat less fluid-like behavior that would be associated with more resistance to flow.

In photoactivated optoGEF embryos, although the average cell shape index $\bar{p}$ displays similar trends as in the optoGAP case, the alignment index *Q* shows qualitatively different behavior compared to control or optoGAP embryos (Fig. 2*A*,*C,D*). Indeed, the cell shape alignment *Q* remained high throughout the process, and did not relax back down to low levels as observed in controls. Comparing these results to the vertex model predictions suggests that the germband in optoGEF embryos again starts out near the predicted solid-fluid transition line, similar to controls, but takes a path through the *p*-*Q* parameter space over time that follows along the transition line instead of relaxing deeper into the fluid-like region (Fig. 2*G*), possibly consistent with significantly less fluid-like behavior and more resistance to flow.

To compare the predicted tissue mechanical properties in the control, optoGEF, and optoGAP groups, we measured the distance to the predicted solid-fluid transition line in the *p*-*Q* parameter space. During the rapid phase of tissue elongation, the distance to the transition line was reduced in optoGAP (P = 0.05) and significantly reduced in optoGEF (P = 0.005) compared to in control embryos (Fig. 2*E*). Taken together, these findings suggest that tissue mechanical properties, which capture how a tissue resists flowing under an applied force, are altered by both activation (optoGEF) and inactivation (optoGAP) of Rho signaling in the germband. In both cases, the germband is predicted to be less fluid-like than in control embryos, which is consistent with the observed reduction in cell rearrangements and tissue flow. However, these results are not sufficient to explain why we observe fewer cell rearrangements in optoGAP compared to optoGEF embryos, despite the prediction of even less fluid-like behavior in the optoGEF case.

Patterns of Rho signaling influence the planar polarized patterns of myosin localization at cell junctions thought to drive tissue flow

We wondered if differences in the mechanical forces driving tissue flow might help to account for the cell rearrangement rates and tissue flows in optoGEF and optoGAP embryos. During germband extension, Rho-kinase (Rok) is necessary for the formation of planar polarized patterns of myosin II localization and activity (14, 32, 36, 37) that are thought to provide driving forces for cell rearrangements and tissue flow during axis elongation (14, 15, 19, 21, 24, 38). To test if myosin-generated driving forces are disrupted, we examined Rok and myosin II localization in photoactivated optoGEF and optoGAP embryos (Fig. 3).

First, we assessed the effects of optogenetic manipulation of Rho1 on Rok localization using a Venus-tagged Rho-kinase^{K116A} transgene (32). In photoactivated control embryos, Rok localized at cell-cell contacts with enhanced accumulation at “vertical” edges between anterior and posterior cell neighbors (AP edges) compared to “horizontal” edges between dorsal and ventral cell neighbors (DV edges) (Fig. 3*D*), similar to in wild-type embryos (32). In photoactivated optoGEF embryos, the localization pattern of Rok was strongly disrupted, with Rok accumulating in clusters in the medial-apical domain of cells (Fig. 3*E*). In contrast, in photoactivated optoGAP embryos, Rok localized at cell-cell contacts, similar to in controls, but the overall levels were decreased and the planar polarized pattern appeared to be disrupted (Fig. 3*F*). Thus, perturbations to Rho1 in optoGEF and optoGAP embryos altered the localization pattern of Rok in the germband.

Next, to analyze how optogenetic recruitment of Rho1 regulators at the apical surface of the germband influences myosin II localization patterns, we performed time-lapse confocal imaging of myosin II in optoGEF and optoGAP embryos. We visualized myosin II using an mCherry-tagged myosin regulatory light chain. In optoGEF embryos, we observed that following blue light exposure starting at t = 0 to recruit RhoGEF2 to the cell membrane, myosin rapidly accumulated at the medial-apical cortex of cells (Fig. 3*B*), with a 22 ± 4% increase in medial myosin within 1 min and a 66 ± 14% increase over 5 min (Fig. 3*I*), compared to 3 ± 2% in 1 min and 9% ± 2% in 5 min in control embryos (Fig. 3*A*,*I*). This increase in medial myosin is consistent with the observed changes in Rok localization (Fig. 3*E*). The rapid increase in medial myosin in optoGEF embryos was accompanied by more gradual changes in junctional myosin levels. Myosin localization at AP and DV cell junctions initially increased, following the same trends as in control embryos, before beginning to decrease 3-5 min after the start of blue light exposure (Figs. 3*G-H*), which was delayed compared to the nearly immediate medial accumulation of myosin (Fig. 3*I*). Together, these changes in myosin localization produced a strong decrease in myosin planar polarity within 3 min of blue light exposure (Fig. 3*K*) and led to the formation of a radial pattern of myosin reminiscent of those found in tissues exhibiting apical constriction and invagination.

In contrast, photoactivation of optoGAP in the germband epithelium resulted in gradual decreases in both medial and junctional myosin (Fig. 3*C,G-I*), demonstrating that ectopic RhoGAP71E cell membrane recruitment is sufficient to decrease cortical localization of myosin, which is consistent with the observed changes in Rok localization (Fig. 3*F*) and the role of RhoGAPs in promoting the inactive state of Rho1. This reduction in cortical myosin occurred over a timescale of ~5 min, which was somewhat slower than the rapid increase in medial myosin in optoGEF embryos. The decreased cortical myosin in optoGAP embryos was associated with a decrease in myosin planar polarity compared to in control embryos (Fig. 3*K*). Thus, myosin planar polarity was disrupted in both optoGEF and optoGAP perturbations.

Patterns of Rho signaling influence the anisotropic forces at cell junctions thought to drive tissue flow

Next, we tested if the altered myosin localization patterns in photoactivated optoGEF and optoGAP embryos resulted in changes to the anisotropic mechanical forces in the tissue, which are thought to be a driving force for germband tissue flow. We used a laser to ablate individual junctional domains at the contacts between neighboring cells (Figs. 4*A,B*) (22, 23, 39–41). Retraction of the tissue away from the ablation site reflects the mechanical tension in the tissue prior to ablation, with the initial retraction velocity being proportional to tension and inversely related to viscous drag. The decreased myosin planar polarity in photoactivated optoGEF and optoGAP embryos would be predicted to result in reduced anisotropy in forces along AP compared to DV cell junctions. In wild-type control embryos, the mean initial retraction velocities were 0.36 ± 0.04 μm/s at AP junctions and 0.11 ± 0.03 μm/s at DV junctions (Fig. 4*C,D*), producing a significant mechanical anisotropy in the tissue (comparison between AP and DV velocities, $P = 9 \times 10^{-6}$, *t*-test) (Fig. 4*E*), consistent with previous studies of mechanical anisotropy in the germband of wild-type embryos (22, 23, 25). In contrast, the mechanical anisotropies in photoactivated optoGEF and optoGAP embryos were reduced (Fig. 4*C-E*), such that the differences between velocities at AP junctions and at DV junctions were less significant ($P = 0.04$, $P = 0.16$ respectively, *t*-test), consistent with the reduced myosin planar polarity in these tissues.

Taken together, these results demonstrate that optogenetic activation or inactivation of Rho signaling nearly abolishes myosin planar polarity across the germband and disrupts the anisotropic contractile tensions associated with myosin activity at cell junctions, helping to explain why cell rearrangements are reduced in both perturbations. However, these results do not fully

explain the differences in the defects observed in the optoGEF and optoGAP embryos. In optoGAP embryos, the germband is predicted to be less fluid-like than in wild-type embryos, and the near abolishment of planar polarized forces from myosin activity results in fewer cell rearrangements and reduced tissue flow. However, in optoGEF embryos, myosin planar polarity is also nearly abolished, and the tissue is predicted to be even less fluid-like, but we observe significantly more cell rearrangements initiated than in the optoGAP case. Furthermore, the cell rearrangements in optoGEF embryos appear to be less productive at contributing to convergent extension, as the final extent of germband tissue elongation is similar in optoGEF and optoGAP embryos.

Rho signaling tunes myosin-dependent forces arising in the medial-apical domain of cells during convergent extension

We wondered what additional features of cell behaviors might be contributing to these distinct defects in the germband of photoactivated optoGEF and optoGAP embryos. One notable feature of myosin II localization in the optoGEF embryos is the significantly enhanced accumulation of myosin at the medial-apical domain of cells (c.f. Fig 3*B,I*). To test how this enhanced medial-apical myosin in optoGEF embryos influences mechanical tensions in the tissue that might contribute to cell rearrangements, we used a laser to ablate myosin in the medial-apical domains of individual cells (Figs. 5*A,B*).

In optoGEF embryos after 5 min of photoactivation, ablation in the medial apical domain in a single cell led to dramatic retraction of the surrounding tissue along both the AP and DV axes (Fig. 5*A,B*), which was significantly enhanced compared to medial ablations in wild-type embryos (P = 0.018) and optoGAP embryos (P = 0.009), in which there was less medial myosin present (Fig. 5*A*). In addition, tissue retraction in optoGEF embryos was more isotropic than in controls. In contrast, medial ablations in photoactivated optoGAP embryos, resulted in retractions more similar in magnitude to control embryos (P = 0.39) (Fig. 5*A,B*). These results indicate that the myosin accumulating at the apical cortex of germband cells in optoGEF embryos is actively generating contractile forces contributing to mechanical tension in the tissue and that these tensions are more isotropic than in control embryos.

In a prior study, our group demonstrated that the enhanced medial-apical myosin pool in activated optoGEF cells shows dynamic pulsing behavior that is correlated with enhanced apical cell area fluctuations (27). Taken together with the current laser ablation studies, our findings suggest that Rho signaling tunes pulsatile contractile forces originating from the medial-apical domain of cells in the germband and that these forces might promote cell rearrangement. This is consistent with recent studies highlighting a potential role for active tension fluctuations in promoting cell rearrangement by helping cells overcome the collective energy barrier associated with cell shape changes during this process (42, 43). Such a mechanism is consistent with the increased cell rearrangement rates in the optoGEF compared to optoGAP perturbations.

Optogenetic manipulation of Rho disrupts distinct aspects of cell rearrangements.

To gain further insight into how these perturbations to tissue mechanical properties and myosin-dependent driving forces influence cell rearrangements and tissue fluidity, we analyzed three distinct steps in cell rearrangement: cell edge contraction, vertex resolution, and new cell edge growth. We hypothesized that manipulation of Rho1, by increasing Rho1 activity (optoGEF) or decreasing Rho1 activity (optoGAP), might affect the rate or spatial organization of these steps in cell rearrangement, leading to the observed changes in cell rearrangement rates and tissue-level flow.

First, we examined whether activation of optoGEF or optoGAP across the tissue altered the speed of cell rearrangements that were initiated. In photoactivated optoGAP embryos, the median speed of contraction of AP or "vertical" cell edges between anterior and posterior cell neighbors (1.12 μm/min) was reduced compared to in control embryos (1.48 μm/min) (*P* = 0.013) (Fig. 6*A*), and the median rate for a high order vertex to resolve to form a DV cell edge was also reduced (0.11 min^{-1}) compared to in control embryos (0.35 min^{-1}) (*P* =0.02) (Fig. 6*B,F,H).* In addition, the median rate of growth of newly formed DV cell edges was decreased in optoGAP (0.93 μm/min) compared to in control embryos (1.26 μm/min) (*P*=0.03) (Fig. 6*C*), consistent with a role for actomyosin contractility both in edge contraction and in vertex resolution (14, 15, 17, 19, 22, 23, 25, 44). In contrast, the speeds of cell rearrangements were not significantly faster in photoactivated optoGEF embryos compared to in controls (Fig. 6*A*-*C*,*G*), suggesting that the increased myosin activity at the cell cortex in optoGEF embryos was not translated into significantly faster cell rearrangements once initiated.

We also analyzed how the altered Rho1 activity in photoactivated optoGEF and optoGAP embryos influenced the spatial organization of cell rearrangements. In control embryos, 97% of vertices formed through contraction of an AP cell edge went on to resolve and form a DV cell edge, to produce a productive rearrangement (Fig. 6*D,F*) consistent with previous studies of cell rearrangement (14, 15, 17, 25, 33). The remaining 3% of vertices failed to resolve within 10 min after the formation of the vertex. In contrast, the percentage of vertices that resolved to form DV edges was reduced to 82% in photoactivated optoGEF embryos (*P* = 0.14) and 60% in photoactivated optoGAP embryos (*P* = 0.005) (Fig. 6*D*). In optoGEF embryos, the remaining 18% of vertices resolved to reform AP cell edges, resulting in unproductive cell rearrangement. In optoGAP embryos, 16% of vertices resolved to reform AP cell edges and 24% did not resolve. In addition, we observed that new junctions formed during cell rearrangement in optoGEF embryos exhibited a disruption in new edge orientation. We observed a higher percentage of new edges forming at 30-60º ("diagonal" to the AP axis) compared to in control and optoGAP embryos (Fig. 6*E,G*), suggesting that the spatial orientation of rearrangements was disrupted by these perturbations.

Thus, inactivation of Rho1 in optoGAP embryos resulted in slower and significantly fewer completed cell rearrangements compared to control embryos, consistent with both a reduction in the overall levels and a disruption to the anisotropy of the myosin-generated forces driving tissue flow. In contrast, activation of Rho1 in optoGEF embryos resulted in less severe defects in the number and speed of rearrangements, but the rearrangements that did initiate were poorly oriented, which may explain why rearrangements in these embryos were less productive at producing tissue-level elongation (c.f. Fig. 1*C,F*). The increased cell rearrangement rates in optoGEF compared to optoGAP perturbations, might reflect the enhanced pulsatile medial-apical myosin contractility in these cells, which have the potential to promote cell rearrangements, especially in the absence of strong myosin planar polarity patterns. Consistent with this picture, cell rearrangements in optoGEF cells with enhanced medial myosin, which produced more isotropic mechanical tensions in the tissue, were in effect more "randomly" oriented within the tissue.

Taken together, these finding demonstrate that optogenetic activation or inactivation of Rho1 across the apical surface of the germband tissue produces distinct defects in the cell behaviors that contribute to convergent extension, directly linking patterns of upstream Rho1 activity and downstream actomyosin contractility to the ability of the tissue to deform and flow through cell rearrangements.

CONCLUSIONS

Our results demonstrate that actomyosin activity influences *both* the anisotropic forces driving flow and the predicted tissue mechanical properties resisting flow in the germband epithelium during *Drosophila* body axis elongation. These dual roles for actomyosin in tissue flow mechanics lead to complex effects of Rho1 activity and actomyosin contractility on the final tissue-level flow. In particular, either increasing (optoGEF) or decreasing (optoGAP) Rho1 activity in the germband reduces overall tissue elongation and produces tissues predicted to be less fluid-like than controls. Moreover, these perturbations have distinct effects on myosin localization patterns, tissue tensions, cell rearrangement rates, and cell rearrangement orientation. Our findings reveal that planar polarized patterns of junctional myosin are required for rapid cell rearrangements *and* tissue-level elongation, while more isotropic patterns of medial-apical myosin are sufficient to promote rapid rearrangements but do not orient those rearrangements to produce tissue-level flows in this context. Future work will further explore how junctional and medial myosin pools work together to tune tissue mechanics in the germband and in other developing epithelia. In addition, to elucidate the origins of solid-fluid tissue mechanical properties, the contributions of cellular adhesive machineries and their interplay with the actomyosin cytoskeleton will need to be investigated. Ultimately, to understand how emergent tissue mechanics and flows are regulated in space and time across the developing embryo to generate functional three-dimensional embryonic structure, we will need to identify the master upstream regulators that tune and coordinate force generation and tissue mechanical properties to achieve both the local cell structure and global tissue shape required for proper function. The approaches and findings we report here will be useful in this endeavor.

MATERIALS AND METHODS

Fly lines and genetics. Embryos were maintained at 23ºC and experiments were performed at room temperature (~ 21ºC). The fly stock w[*]; P[w+, UASp>CIBN-caax]; was generated in this study by PCR amplification of the CIBN-caax fragment from plasmid pPW_CIBNcaax (gift from Stefano De Renzis). The fragment was cloned into the pENTR/D-Topo vector (Life Technologies) and recombined into UASp-attB destination vector (gift from F. Wirtz-Peitz) using the Gateway cloning system (Life Technologies) for subsequent expression using the Gal4/UAS system (45). The plasmid was inserted into the attP40 site on chromosome II to generate transgenic flies (Bestgene).

The fly stocks w*;; w+, UASp>mCherry-CRY2PHR-RhoGEF2 and w*;; w+, UASp>mCherry-CRY2PHR-RhoGAP71E were crossed with w*; P[w+, UASp>CIBN-pmGFP]/Cyo; Sb/TM3,Ser (gift of Stefano De Renzis, EMBL, Heidelberg, Germany). The stocks w*;; w+, UASp> CRY2PHR-RhoGEF2 and w*;; w+, UASp> CRY2PHR-RhoGAP71E were crossed with w*; P[w+, UASp>CIBN-pmGFP]/Cyo; Sb/TM3,Ser (gift of Stefano De Renzis, EMBL, Heidelberg, Germany) or w*; w+, UASp>CIBN-caax;. The constructs were expressed using the maternal α-tubulin matα-tub15 or matα-tub67 Gal4-VP16 drivers (mat67, mat15, gift of D. St Johnston).

To visualize myosin II, mat15 and sqh>sqh-mCherry (BDSC 59024, donated by Beth Stronach and Elane Fishilevich) were recombined on chromosome III. For Rho-kinase (Rok) visualization, mat15 and sqh>Venus-Rok^{K116A} (gift of Jennifer Zallen) (32) were recombined on chromosome III. To protect the embryos from light, crosses were maintained in the dark, and fly sorting was performed in the dark on a stereoscope equipped with Red 25 Kodak Wratten Filter.

Embryos were the progeny of females of the following genotypes:

UASp>CIBN-pmGFP/mat67 (II); sqh>sqh-mCherry/+ (III)
sqh> Venus-Rok^{K116A} (III)
UASp>CIBN-pmGFP/+ (II); UASp>mCherry-CRY2PHR-RhoGEF2/mat15 (III)
UASp>CIBN-pmGFP/+ (II); UASp>CRY2PHR-RhoGEF2/sqh>sqh-mCherry, mat15 (III)
UASp>CIBN-caax/+ (II); UASp>CRY2PHR-RhoGEF2/ sqh>Venus-Rok^{K116A}, mat15 (III)
UASp>CIBN-pmGFP/mat67 (II); UASp>mCherry-CRY2PHR-RhoGAP71E/mat15 (III)
UASp>CIBN-pmGFP/mat67 (II); UASp>CRY2PHR-RhoGAP71E/sqh>sqh-mCherry, mat15 (III)
UASp>CIBN-caax/mat67 (II); UASp>CRY2PHR-RhoGAP71E/ sqh>Venus-Rok^{K116A}, mat15 (III)

Fly stocks used in this study:
w*; w+, UASp>CIBN-pmGFP/CyO; Sb/TM3,Ser (Stefano De Renzis, EMBL, Heidelberg, Germany)
w*; w+, UASp> CIBN-caax; (this study)
w*;; w+, UASp>mCherry-CRY2PHR-RhoGEF2/TM3,Sb
w*;; w+, UASp>CRY2PHR-RhoGEF2/TM3,Sb
w*;; w+, UASp>mCherry-CRY2PHR-RhoGAP71E/TM3,Sb
w*;; w+, UASp>CRY2PHR-RhoGAP71E/TM3,Sb
w*;; sqh>sqh-mCherry
w*; w+, UASp>CIBNpm-GFP, mat67; sqh>sqh-mCherry
w*;; mat15
w*; mat67; mat15
w*;; sqh>sqh-mCherry, mat15
w*; mat67; sqh>sqh-mCherry, mat15
w*;; sqh>Venus-Rok^{K116A}
w*;; sqh>Venus-Rok^{K116A},mat15
w*; mat67; sqh>Venus-Rok^{K116A} (III)

Embryo preparation. Embryos were prepared and collected in a dark room illuminated with red light. Embryos in early stage 6 were dechorionated with 50% bleach for 2 min, washed with water, and mounted using a mixture 50:50 of halocarbon oil 27:700 on a custom-made imaging chamber between an oxygen-permeable membrane (YSI Incorporated) and a glass coverslip.

Imaging. Embryos were positioned ventrolaterally for observation of the germband. Photoactivation and imaging was performed with a Zeiss LSM 880 confocal microscope with Airyscan detector and equipped with an Argon laser for 488 nm excitation and a diode laser for 561 nm excitation (Carl Zeiss, Germany). Imaging was performed with C-Apo 40X/1.2 NA water-immersion or Plan-Apo 63X/1.40 NA Oil-immersion objectives (Carl Zeiss, Germany). The bright field illumination light was filtered through a Red 25 Kodak Wratten Filter to prevent unwanted photoactivation. Image acquisition was performed with ZEN black software (Carl Zeiss, Germany) using the standard LSM mode unless otherwise noted. For myosin II and Rok imaging, the Airyscan FAST module was utilized. Images were acquired as 10 μm z-stacks with a 1 μm z-step (40X objective, LSM mode) or a 0.7 μm z-step (63X objective, Airyscan FAST), beginning at the apical side of the tissue. Z-stacks were acquired every 15 s. Photoactivation was achieved by scanning with blue laser light (λ = 488 nm) over the same ventrolateral region of the germband that was being imaged, at every imaging z-plane and time-step.

Image analysis. Confocal time-lapse movies of the cell outlines visualized using CIBN-pmGFP, were projected using the ImageJ distribution Fiji software (46, 47) and used to calculate tissue elongation during body axis elongation using the particle image velocimetry (PIV) software PIVlab version 1.41 (48) in MATLAB as previously described (25, 48). To quantify vertex coordination number and number of rearrangements per cell, movies with fluorescently-tagged cell

membranes were segmented using the SEGGA tissue segmentation and analysis software (16). The instantaneous rate of rearrangements was calculated as a moving average of the cell rearrangement rate over 1.5 min windows.

Signal intensity quantification. For myosin II analysis, still frames shown and confocal movies analyzed correspond to the maximum intensity projections of 5 µm at the apical side of the tissue, starting apically. Images were processed and analyzed using the ImageJ distribution Fiji software (46, 47). The mean junctional myosin intensity at each cell edge was quantified manually using 6 pixel-wide lines (excluding vertex regions) in a 40 µm square region, and the intensity and orientation of each edge was obtained. Medial apical myosin intensity was quantified manually as the mean intensity in a polygon manually drawn just inside the cell membrane outline. At least 10 cells and 40 junctions were analyzed per embryo (Fig. 3). Planar polarity was obtained as the ratio of the mean intensity of AP ("vertical") edges to the mean intensity of DV ("horizontal") edges for each embryo (Fig. 3).

Cell rearrangement analysis. Cell rearrangements were manually analyzed for 10-25 vertical cell edges per embryo (n=48-69 edges in total from 3-5 embryos per genotype). AP edges were selected at the beginning of axis elongation, and their fate was tracked over 30 min. Edge contraction rate was calculated from changes in edge length during the 2 min before vertex formation. New edge growth rate and orientation were calculated over the 2 min following vertex resolution. Vertex lifetime corresponds to the time between when the edge contracts to a vertex and when the new edge is > 1 µm long. Vertices that did not resolve corresponded to AP edges that contracted to a vertex but did not resolve to form a new edge within the tracking time-window (vertices that formed >20min after the start of the analysis window were not included in the analysis). Vertices that resolved in the wrong direction correspond to AP edges that contracted to a vertex and then resolved to reform an AP cell edge instead of forming a new contact between dorsal and ventral cell neighbors.

Laser ablation. Samples for ablation studies were prepared in a dark room illuminated with red light. Embryos were dechorionated and mounted in a 50:50 mixture of halocarbon oils 27 and 700 within a custom-made imaging chamber. Embryos expressing optogenetic tools were photoactivated with blue light from an Argon laser (λ = 488 nm) at every z-plane (10 µm z-stacks with 1 µm steps) every 15 s per stack during the 5 min prior to ablations. Ablations were performed using a Chameleon Ultra2 laser set to 710 nm on a Zeiss LSM 880 confocal microscope equipped with a Plan-Apo 63X/1.4 NA oil DIC M27 immersion objective. The following laser settings were used for ablation: 60% laser power, 1 iteration, scan speed of 0.0143 ms per pixel, 1.3 µm line. After ablation, single z-plane images were acquired every 1 s for at least 30 s. For vertex retraction measurements following ablation of junctions, the distance between the vertices connected to the ablated edge were manually measured over time. To generate tissue displacement maps, displacements were quantified by particle image velocimetry (PIV) analysis (Matlab PIVlab version 1.41) (48) using a 5 by 5 grid (3.3 µm between grid points) in a 174 μm^2 region surrounding the ablation point over the course of 30 s following ablation. For radial plots, mean displacements were calculated in 60º angular bins along the anterior, posterior, dorsal, or ventral tissue axes, taking the ablation point as the origin.

Cell shape index and cell shape alignment analysis. Cell outlines were segmented using the SEGGA tissue segmentation and analysis software (16). For each segmented cell within a specified region of interest, the perimeter (*P*) and area (*A*) was measured and the ratio $P/\sqrt{A}$ was calculated. The average shape index $\bar{p}$ is the average value of $P/\sqrt{A}$ for all cells. To account for effects of cell packing disorder, the corrected shape index $\bar{p}_{corr}$ was calculated by subtracting the

term (z-3)/B from $\bar{p}$, where z is the vertex coordination number (average number of cells meeting at a single vertex) and B is 3.85, as previously described (4). To calculate the cell shape alignment Q, the tissue was triangulated as previously described (4, 49). For each triangle, an alignment tensor is calculated. Q is the magnitude of the area-weighted average of the alignment tensors as described in (4, 49). As previously described, the predicted solid-fluid transition line is given by $\bar{p}_{corr} = 3.818 + 4bQ^2$(4), where b=0.6 ± 0.2 based on previously reported vertex model simulation results (49).

Statistical analysis. Data is presented as mean values +/- the standard error of the mean (SEM). We used the nonparametric Kruskal-Wallis test with post-hoc Dunn test to determine P-values unless otherwise noted.

ACKNOWLEDGEMENTS

We thank Nandan Nerurkar for use of microscope and laser facilities for ablation studies, Stefano De Renzis for the UASp>CIBN::pmGFP fly stock, Jennifer Zallen and Frederik Wirtz-Peitz for the UASp-attB destination vectors, the Bloomington Drosophila Stock Center (BDSC) for fly stocks, and members of the Kasza Lab for helpful discussion and comments on the manuscript. This work was supported by the National Institute of General Medical Sciences of the National Institutes of Health Award Number R35GM138380 (to K.E.K.); Eunice Kennedy Shriver National Institute of Child Health & Development of the National Institutes of Health Grant F31HD105405 (to C.C); National Science Foundation Graduate Research Fellowship (to A.B.D.). K.E.K holds a Career Award at the Scientific Interface from the Burroughs Wellcome Fund, a Clare Boothe Luce Professorship, and a Packard Fellowship. M.H.P holds a Career Award at the Scientific Interface from the Burroughs Wellcome Fund.

REFERENCES

1. Herrera-Perez, R.M., and K.E. Kasza. 2018. Biophysical control of the cell rearrangements and cell shape changes that build epithelial tissues. *Curr. Opin. Genet. Dev.* 51:88–95.
2. Walck-Shannon, E., and J. Hardin. 2014. Cell intercalation from top to bottom. *Nat. Rev. Mol. Cell Biol.* 15:34–48.
3. Tetley, R.J., and Y. Mao. 2018. The same but different: cell intercalation as a driver of tissue deformation and fluidity. *Philos. Trans. R. Soc. B Biol. Sci.* 373:20170328.
4. Wang, X., M. Merkel, L.B. Sutter, G. Erdemci-Tandogan, M.L. Manning, and K.E. Kasza. 2020. Anisotropy links cell shapes to tissue flow during convergent extension. *Proc. Natl. Acad. Sci.* 117:13541–13551.
5. Tetley, R.J., M.F. Staddon, D. Heller, A. Hoppe, S. Banerjee, and Y. Mao. 2019. Tissue fluidity promotes epithelial wound healing. *Nat. Phys.* 15:1195–1203.
6. Jain, A., V. Ulman, A. Mukherjee, M. Prakash, M.B. Cuenca, L.G. Pimpale, S. Münster, R. Haase, K.A. Panfilio, F. Jug, S.W. Grill, P. Tomancak, and A. Pavlopoulos. 2020. Regionalized tissue fluidization is required for epithelial gap closure during insect gastrulation. *Nat. Commun.* 11:5604.
7. Banavar, S.P., E.K. Carn, P. Rowghanian, G. Stooke-Vaughan, S. Kim, and O. Campàs. 2021. Mechanical control of tissue shape and morphogenetic flows during vertebrate body axis elongation. *Sci. Rep.* 11:8591.
8. Mongera, A., P. Rowghanian, H.J. Gustafson, E. Shelton, D.A. Kealhofer, E.K. Carn, F. Serwane, A.A. Lucio, J. Giammona, and O. Campàs. 2018. A fluid-to-solid jamming transition underlies vertebrate body axis elongation. *Nature*. 561:401–405.
9. Kasza, K.E., and J.A. Zallen. 2011. Dynamics and regulation of contractile actin-myosin networks in morphogenesis. *Curr. Opin. Cell Biol.* 23:30–38.
10. Heisenberg, C.P., and Y. Bellaïche. 2013. Forces in tissue morphogenesis and patterning. *Cell*. 153:948–962.
11. Martin, A.C. 2010. Pulsation and stabilization: contractile forces that underlie morphogenesis. *Dev. Biol.* 341:114–125.
12. Bi, D., J.H. Lopez, J.M. Schwarz, and M.L. Manning. 2015. A density-independent rigidity transition in biological tissues. *Nat. Phys.* 11:1074–1079.
13. Irvine, K.D., and E. Wieschaus. 1994. Cell intercalation during *Drosophila* germband extension and its regulation by pair-rule segmentation genes. *Development*. 120:827–841.
14. Bertet, C., L. Sulak, and T. Lecuit. 2004. Myosin-dependent junction remodelling controls planar cell intercalation and axis elongation. *Nature*. 429:667–671.
15. Blankenship, J.T., S.T. Backovic, J. Sanny, O. Weitz, and J.A. Zallen. 2006. Multicellular Rosette Formation Links Planar Cell Polarity to Tissue Morphogenesis. *Dev. Cell*. 11:459–470.
16. Farrell, D.L., O. Weitz, M.O. Magnasco, and J.A. Zallen. 2017. SEGGA: a toolset for rapid automated analysis of epithelial cell polarity and dynamics. *Development*. 144:1725–1734.
17. Kasza, K.E., S. Supriyatno, and J.A. Zallen. 2019. Cellular defects resulting from disease-related myosin II mutations in *Drosophila*. *Proc. Natl. Acad. Sci.* 116:22205–22211.
18. Butler, L.C., G.B. Blanchard, A.J. Kabla, N.J. Lawrence, D.P. Welchman, L. Mahadevan, R.J. Adams, and B. Sanson. 2009. Cell shape changes indicate a role for extrinsic tensile forces in *Drosophila* germ-band extension. *Nat. Cell Biol.* 11:859–864.
19. Collinet, C., M. Rauzi, P.-F. Lenne, and T. Lecuit. 2015. Local and tissue-scale forces drive oriented junction growth during tissue extension. *Nat. Cell Biol.* 17:1247–1258.
20. Lye, C.M., G.B. Blanchard, H.W. Naylor, L. Muresan, J. Huisken, R.J. Adams, and B.

Sanson. 2015. Mechanical coupling between endoderm invagination and axis extension in *Drosophila*. *PLoS Biol.* 13:e1002292.
21. Zallen, J.A., and E. Wieschaus. 2004. Patterned gene expression directs bipolar planar polarity in *Drosophila*. *Dev Cell*. 6:343–355.
22. Rauzi, M., P. Verant, T. Lecuit, and P.-F. Lenne. 2008. Nature and anisotropy of cortical forces orienting *Drosophila* tissue morphogenesis. *Nat. Cell Biol.* 10:1401–1410.
23. Fernandez-Gonzalez, R., S. Simões, J.C. Röper, S. Eaton, and J.A. Zallen. 2009. Myosin II Dynamics Are Regulated by Tension in Intercalating Cells. *Dev. Cell*. 17:736–743.
24. Rauzi, M., P.-F. Lenne, and T. Lecuit. 2010. Planar polarized actomyosin contractile flows control epithelial junction remodelling. *Nature*. 468:1110–1114.
25. Kasza, K.E., D.L. Farrell, and J.A. Zallen. 2014. Spatiotemporal control of epithelial remodeling by regulated myosin phosphorylation. *Proc. Natl. Acad. Sci.* 111:11732–11737.
26. Munjal, A., J.M. Philippe, E. Munro, and T. Lecuit. 2015. A self-organized biomechanical network drives shape changes during tissue morphogenesis. *Nature*. 524:351–355.
27. Herrera-Perez, R.M., C. Cupo, C.J. Allan, A. Lin, and K.E. Kasza. 2021. Using optogenetics to link myosin patterns to contractile cell behaviors during convergent extension. *Biophys. J.* 120:1–16.
28. Kennedy, M.J., R.M. Hughes, L.A. Peteya, J.W. Schwartz, M.D. Ehlers, and C.L. Tucker. 2010. Rapid blue-light–mediated induction of protein interactions in living cells. *Nat. Methods*. 7:973–975.
29. Idevall-Hagren, O., E.J. Dickson, B. Hille, D.K. Toomre, and P. De Camilli. 2012. Optogenetic control of phosphoinositide metabolism. *Proc. Natl. Acad. Sci.* 109:E2316–E2323.
30. Guglielmi, G., J.D. Barry, W. Huber, and S. De Renzis. 2015. An Optogenetic Method to Modulate Cell Contractility during Tissue Morphogenesis. *Dev. Cell*. 35:646–660.
31. Izquierdo, E., T. Quinkler, and S. De Renzis. 2018. Guided morphogenesis through optogenetic activation of Rho signalling during early *Drosophila* embryogenesis. *Nat. Commun.* 9:2366.
32. Simões, S., J.T. Blankenship, O. Weitz, D.L. Farrell, M. Tamada, R. Fernandez-Gonzalez, and J.A. Zallen. 2010. Rho-kinase directs bazooka/Par-3 planar polarity during *Drosophila* axis elongation. *Dev. Cell*. 19:377–388.
33. Paré, A.C., A. Vichas, C.T. Fincher, Z. Mirman, D.L. Farrell, A. Mainieri, and J.A. Zallen. 2014. A positional Toll receptor code directs convergent extension in *Drosophila*. *Nature*. 515:523–527.
34. Park, J.-A., J.H. Kim, D. Bi, J.A. Mitchel, N.T. Qazvini, K. Tantisira, C.Y. Park, M. McGill, S.-H. Kim, B. Gweon, J. Notbohm, R.J. Steward, S. Burger, S.H. Randell, A.T. Kho, D.T. Tambe, C. Hardin, S.A. Shore, E. Israel, D.A. Weitz, D.J. Tschumperlin, E.P. Henske, S.T. Weiss, M.L. Manning, J.P. Butler, J.M. Drazen, and J.J. Fredberg. 2015. Unjamming and cell shape in the asthmatic airway epithelium. *Nat. Mater.* 14:1040–1048.
35. Mitchel, J.A., A. Das, M.J. O'Sullivan, I.T. Stancil, S.J. DeCamp, S. Koehler, O.H. Ocaña, J.P. Butler, J.J. Fredberg, M.A. Nieto, D. Bi, and J.-A. Park. 2020. In primary airway epithelial cells, the unjamming transition is distinct from the epithelial-to-mesenchymal transition. *Nat. Commun.* 11:5053.
36. Dawes-Hoang, R.E., K.M. Parmar, A.E. Christiansen, C.B. Phelps, A.H. Brand, and E.F. Wieschaus. 2005. Folded Gastrulation, Cell Shape Change and the Control of Myosin Localization. *Development*. 132:4165–4178.
37. Simões, S., A. Mainieri, and J.A. Zallen. 2014. Rho GTPase and Shroom direct planar polarized actomyosin contractility during convergent extension. *J. Cell Biol.* 204:575–589.
38. Kerridge, S., A. Munjal, J.M. Philippe, A. Jha, A.G. De Las Bayonas, A.J. Saurin, and T. Lecuit. 2016. Modular activation of Rho1 by GPCR signalling imparts polarized myosin II

activation during morphogenesis. *Nat. Cell Biol.* 18:261–270.
39. Hutson, M.S., Y. Tokutake, M.S. Chang, J.W. Bloor, S. Venakides, D.P. Kiehart, and G.S. Edwards. 2003. Forces for morphogenesis investigated with laser microsurgery and quantitative modeling. *Science (80).* 300:145–149.
40. Farhadifar, R., J.C. Roper, B. Aigouy, S. Eaton, F. Julicher, J.C. Röper, B. Aigouy, S. Eaton, and F. Jülicher. 2007. The influence of cell mechanics, cell-cell interactions, and proliferation on epithelial packing. *Curr Biol*. 17:2095–2104.
41. Herrera-Perez, R.M., and K.E. Kasza. 2019. Manipulating the patterns of mechanical forces that shape multicellular tissues. *Physiology*. 34:381–391.
42. Kim, S., M. Pochitaloff, G.A. Stooke-Vaughan, and O. Campàs. 2021. Embryonic tissues as active foams. *Nat. Phys.* 17:859–866.
43. Krajnc, M. 2020. Solid–fluid transition and cell sorting in epithelia with junctional tension fluctuations. *Soft Matter*. 16:3209–3215.
44. Yu, J.C., and R. Fernandez-Gonzalez. 2016. Local mechanical forces promote polarized junctional assembly and axis elongation in *Drosophila*. *Elife*. 5:1–15.
45. Brand, A.H., and N. Perrimon. 1993. Targeted gene expression as a means of altering cell fates and generating dominant phenotypes. *Development*. 118:289–295.
46. Schindelin, J., I. Arganda-Carreras, E. Frise, V. Kaynig, M. Longair, T. Pietzsch, S. Preibisch, C. Rueden, S. Saalfeld, B. Schmid, J.-Y. Tinevez, D.J. White, V. Hartenstein, K. Eliceiri, P. Tomancak, and A. Cardona. 2012. Fiji: an open-source platform for biological-image analysis. *Nat. Methods*. 9:676.
47. Rueden, C.T., J. Schindelin, M.C. Hiner, B.E. DeZonia, A.E. Walter, E.T. Arena, and K.W. Eliceiri. 2017. ImageJ2: ImageJ for the next generation of scientific image data. *BMC Bioinformatics*. 18:529.
48. Thielicke, W., and E.J. Stamhuis. 2014. PIVlab – Towards user-friendly, affordable and accurate digital particle image velocimetry in MATLAB. *J. Open Res. Softw.* 2:e30.
49. Merkel, M., K. Baumgarten, B.P. Tighe, and M.L. Manning. 2019. A minimal-length approach unifies rigidity in underconstrained materials. *Proc. Natl. Acad. Sci.* 116:6560 LP – 6568.

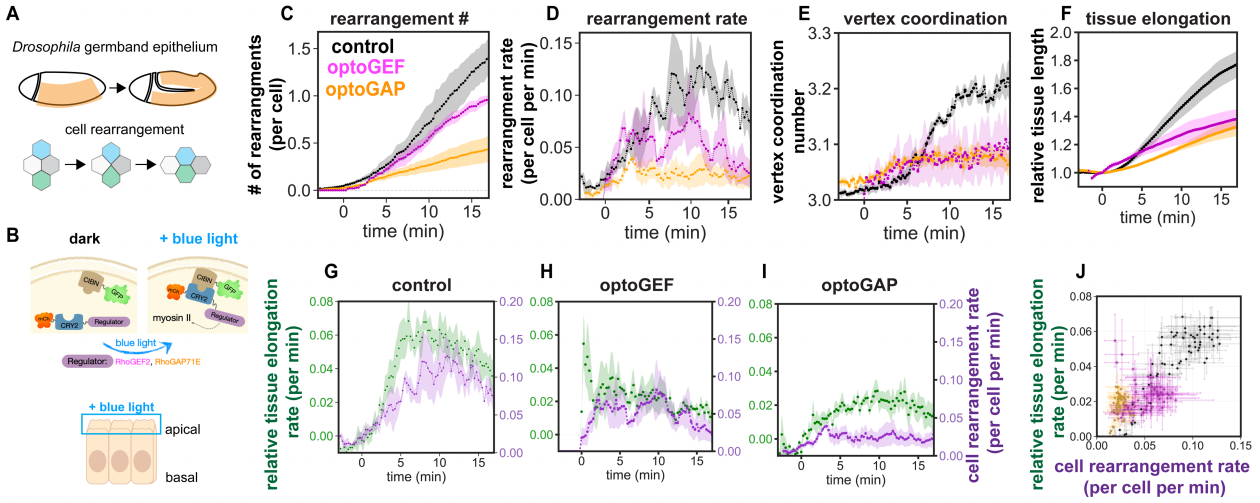

Figure 1. (A) *Top,* Schematic of *Drosophila* body axis elongation. The germband epithelial tissue (orange) narrows and elongates the embryonic body axis in a convergent extension movement driven by oriented cell rearrangements. *Bottom,* Schematic of an oriented cell rearrangement. **(B)** *Top,* Schematic of optogenetic tools. CIBN is tagged to the cell membrane. The light-sensitive PHR domain of CRY2 is fused to upstream myosin II regulators of the Rho/Rho-kinase pathway, RhoGEF2 or RhoGAP71E. Under blue light illumination, CRY2 dimerizes with CIBN and the myosin II regulators accumulate at the cell membrane. *Bottom*, Blue-light illumination of the apical surface of the germband epithelium in the *Drosophila* embryo. **(C)** Number of cell rearrangements initiated in control, optoGEF, and optoGAP embryos, including both T1 processes and higher-order rosette rearrangement events. **(D)** Instantaneous rate of rearrangements per cell per minute. **(E)** Cell vertex coordination number represents the average number of cells meeting at a common vertex across the tissue. **(F)** Elongation of the germband tissue during convergent extension quantified by PIV analysis of time-lapse confocal movies of embryos. The length of the tissue was normalized to the value at $t = 0$. **(G-I)** Instantaneous rates of tissue elongation and cell rearrangements over time for control (G), optoGEF (H), and optoGAP embryos (I). **(J)** Correlation between the instantaneous rates of tissue elongation and cell rearrangement. Each data point represents the mean between embryos at an individual time point. The mean ± SEM between embryos is shown, n=3-5 embryos per genotype.

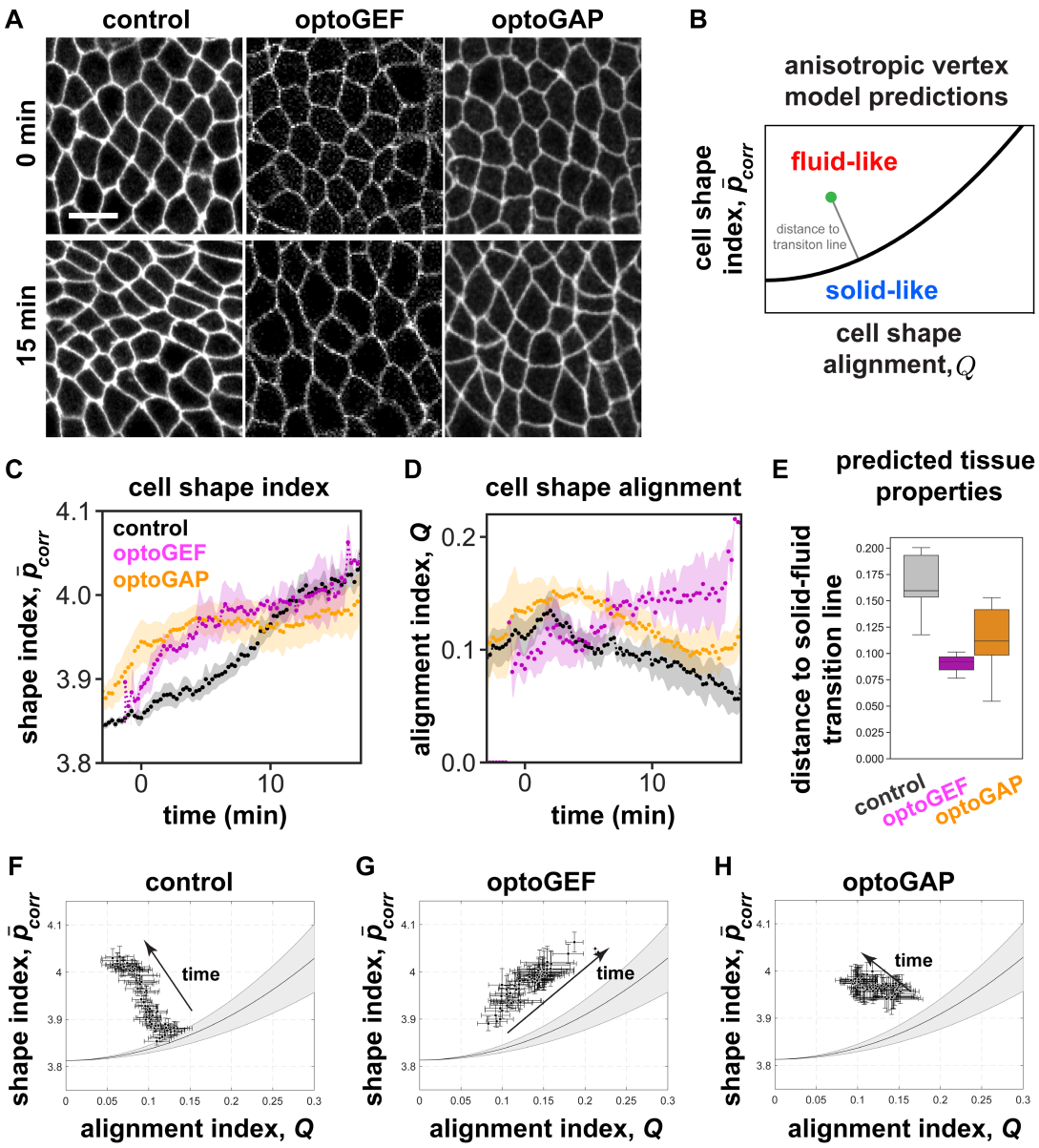

Figure 2. (A) Stills from confocal movies showing cell packings during axis elongation. Anterior, left. Ventral, down. Bar, 10 μm. **(B)** The cell shape index and cell shape alignment can be used to predict tissue mechanical behavior using an anisotropic vertex model. **(C)** The corrected average cell shape index $\bar{p}_{\text{corr}}$ during convergent extension in photoactivated control, optoGEF and optoGAP embryos. $\bar{p}_{\text{corr}}$ is calculated as described in the Materials and Methods section. The mean ± SEM between embryos is shown, n=3-5 embryos per genotype. **(D)** The cell shape alignment index *Q*. The mean ± SEM between embryos is shown, n=3-5 embryos per genotype **(E)** Distance to the predicted solid-fluid transition line, evaluated during the rapid phase of tissue elongation (*t* = 15 min). **(F-H)** Relationship between the corrected averaged cell shape index and cell shape alignment in the tissue for control (H), optoGEF (G) and optoGAP (H) embryos. Each data point represents the mean between embryos at an individual time point, n=3-5 embryos per genotype. Solid line represents the predicted solid-fluid transition line, shaded area represents the range of values for the transition from prior vertex model simulations (see Materials and Methods section).

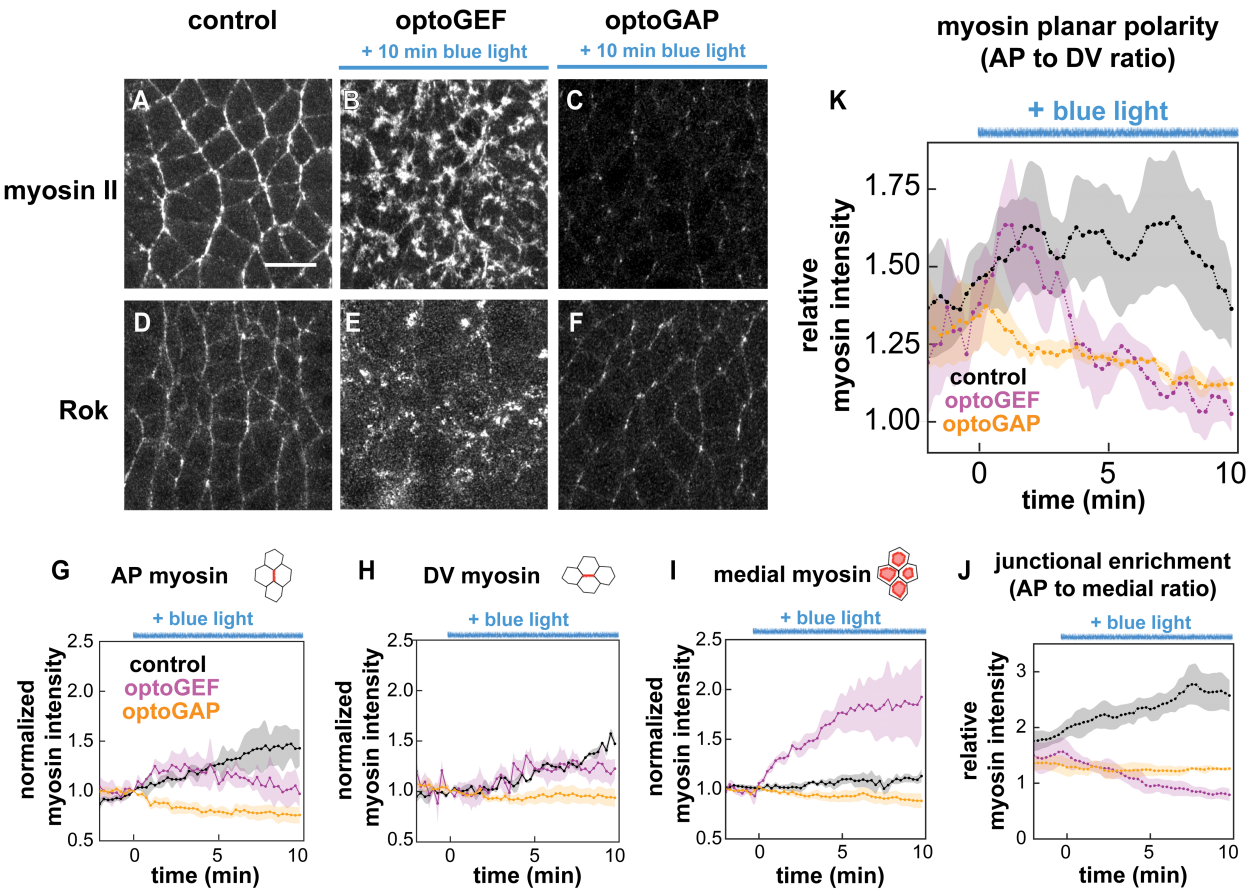

Figure 3. (A-F) Stills from movies of epithelial germband cells during *Drosophila* body axis elongation showing myosin II and Rho-kinase (Rok) localization in control, optoGEF, and optoGAP embryos after continuous activation of the tool for 10 min. Bar, 10 μm. Maximum intensity projection of z-slices in the most apical 5 μm. Myosin II (myosin) was visualized using an mCherry-tagged myosin regulatory light chain (*sqh*) transgene, Rok was visualized using a Venus-tagged Rho-kinase^{K116A} transgene under the myosin regulatory light chain (*sqh*) promoter. **(G-H)** Mean junctional myosin intensity before and during tool activation beginning at t = 0 (duration of blue light exposure indicated by blue line) at AP (*G*) and DV (*H*) junctions. Both optoGEF and optoGAP embryos exhibit decreased junctional myosin accumulation compared to controls, n=3-4 embryos, > 30 junctions/embryo. **(I)** Mean myosin intensity in the medial-apical domain of cells over time. The optoGEF embryos exhibit medial myosin accumulation, while optoGAP embryos show decreased medial myosin following blue light illumination beginning at t = 0. n=3-4 embryos, >10 cells/embryo **(J)** Ratio of mean myosin intensities at AP junctions compared to in the medial apical domain. Ratios for each embryo at each time point were calculated, and the mean ± SEM between embryos is shown. **(K)** Ratio of mean myosin intensities at AP compared to at DV junctions. Myosin planar polarity was disrupted in optoGEF and optoGAP embryos. Ratios for each embryo at each time point were calculated, and the mean ± SEM between embryo is shown.

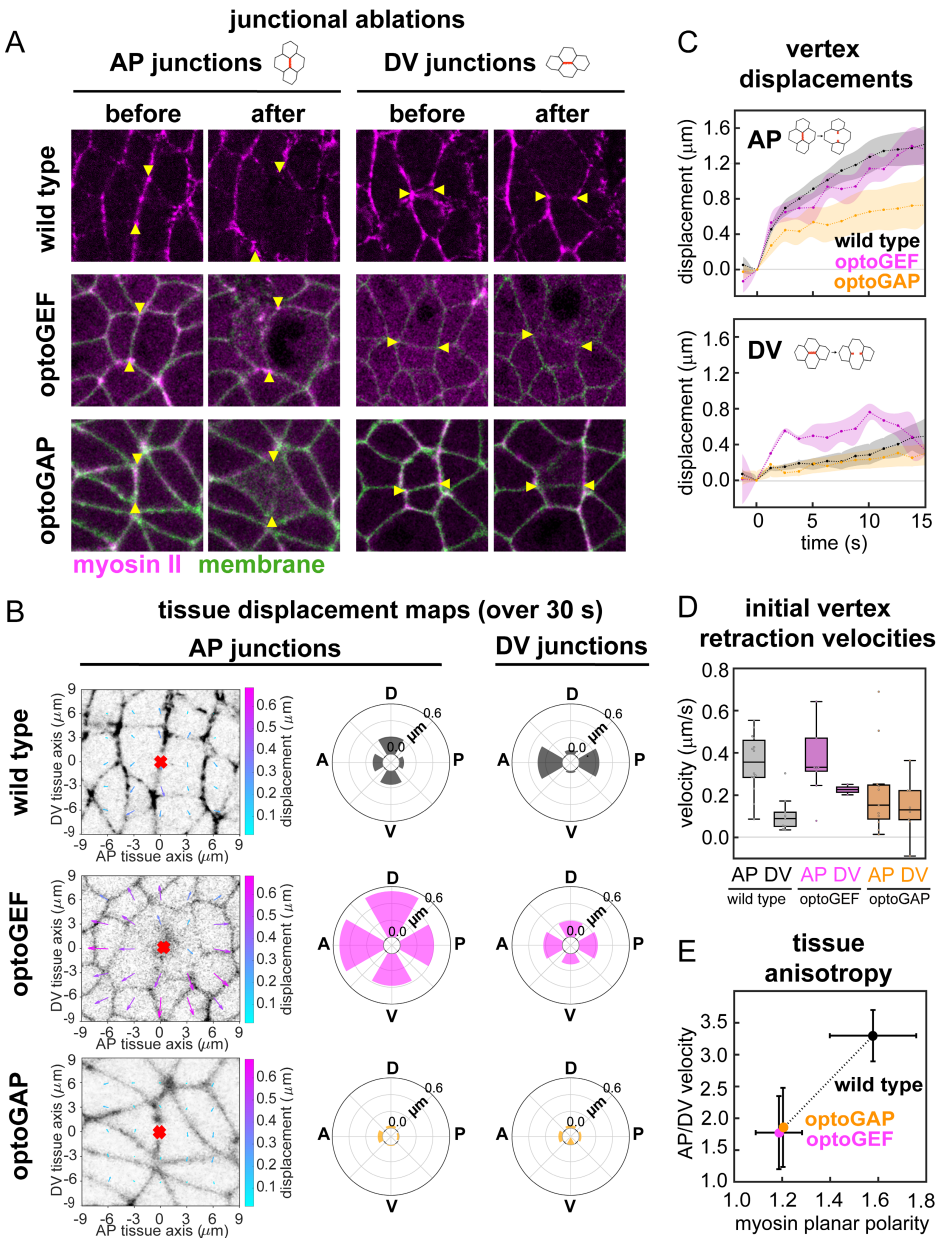

Figure 4. Ablations at cell-cell junctions in optogenetically manipulated germband tissue. **(A)** Cells before (left) and 1 min after (right) ablation. Myosin II (magenta), CIBN-pmGFP (green). Arrowheads indicate the vertices connected to the junction in which the cut was made. Anterior, left. Ventral, down. Image size, 20 x 20 μm. **(B)** Maps of displacements in the surrounding tissue in the 30 s following ablations. The tissue in a 174 μm^2 region surrounding the ablation point (red mark) was analyzed by PIV analysis following ablation. Radial plots show the mean total displacement, averaged over the regions in 60º angular bins, along the anterior, posterior, dorsal, or ventral tissue axes, n = 3-11 ablations per condition. **(C)** Vertex displacements following ablations at AP or DV junctions. Mean ± SEM between junctions is shown, n=10-15 AP, 3-10 DV junctions per condition. **(D)** Initial vertex retraction velocities after ablation. **(E)** Mechanical anisotropy was reduced in optoGEF and optoGAP embryos and correlates with myosin planar polarity at 5 min after optogenetic activation (c.f. Fig. 3*K*). Mechanical anisotropy was calculated as the ratio of mean AP to mean DV peak retraction velocities, n= 3-15 edges per condition.

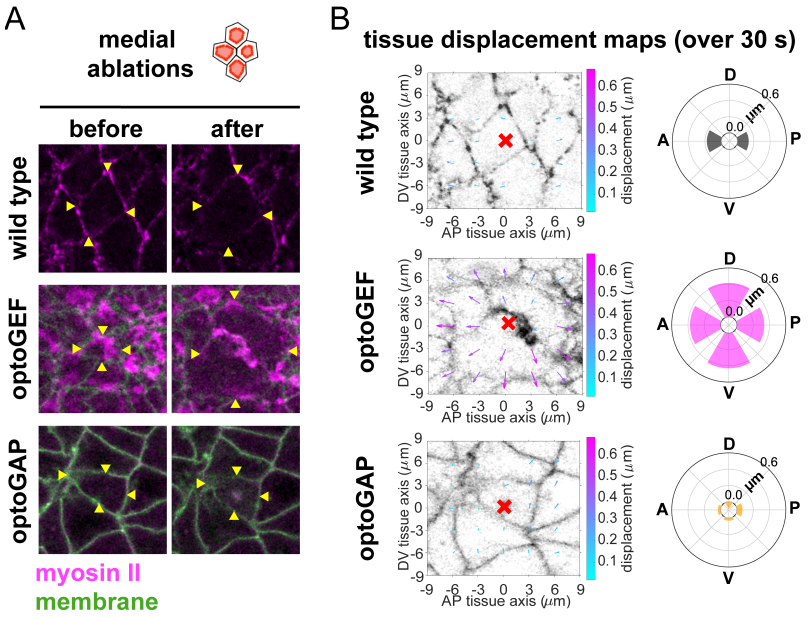

Figure 5. Ablations in the medial-apical domain of cells in optogenetically manipulated germband tissue. (*A*) Cells before (left) and 1 min after (right) ablation. Myosin II (magenta), CIBN-pmGFP (green). Arrowheads indicate the vertices connected to the cell in which the cut was made. Anterior, left. Ventral, down. Image size, 20 μm. (*B*) Maps of displacements in the surrounding tissue in the 30 s following ablations. The tissue in a 174 μm^2 region surrounding the ablation point (red mark) was analyzed by PIV analysis following ablation. Radial plots show the mean total displacement, averaged over the regions in 60º angular bins, along the anterior, posterior, dorsal, or ventral tissue axes, n = 3-11 ablations per condition.

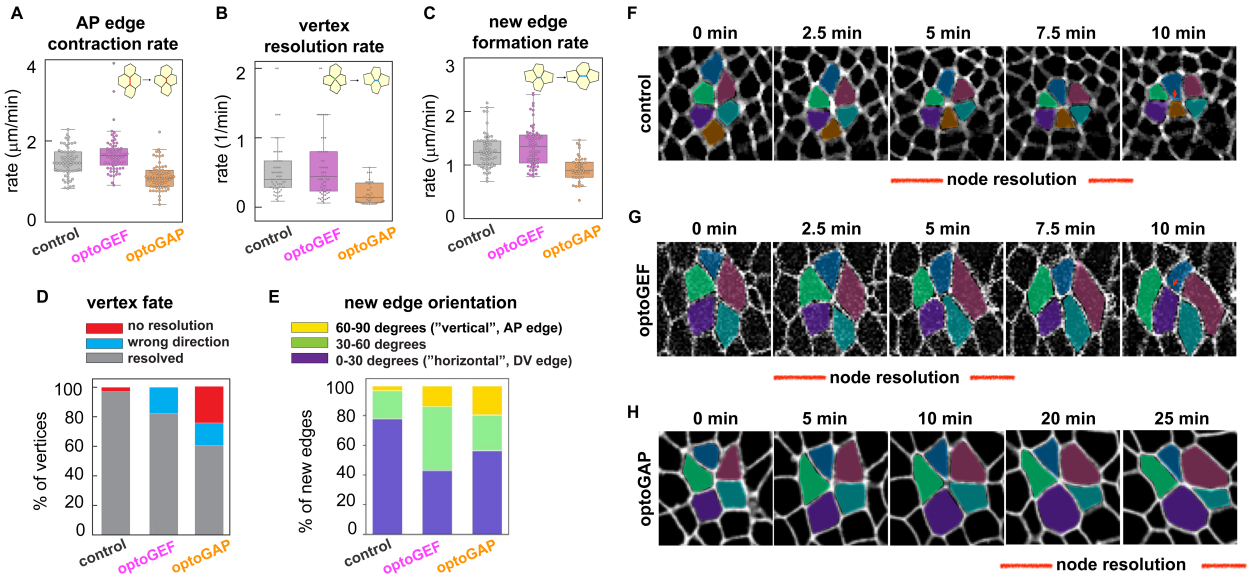

Figure 6. (A-C) AP cell edge contraction rate, vertex resolution rate, and new edge formation rate are reduced in optoGAP embryos compared to control embryos. Each data point represents a cell rearrangement initiated by contraction of an AP edge. n=10-25 edges/embryo from 3-5 embryos (n=48-69 edges per genotype). See details in the Materials and Methods section. **(D)** The fate of vertices formed through contraction of AP cell edges. The optoGAP and optoGEF embryos showed an increased percentage of vertices that did not resolve or aberrantly resolved to reform an AP edge. **(E)** The orientation of newly formed cell edges. While the majority of the new edges in control embryos correspond to edges oriented parallel to the anterior-posterior axis of the embryo (orientation 0-30º), optoGEF embryos showed an increase in edges with diagonal orientation (30-60º). Both optoGEF and optoGAP embryos showed increased numbers of edges that reform in an orientation similar to the initial orientation of AP edges (60-90º). n=3-5 embryos per genotype, 10-25 junctions/embryo. **(F-H)** Still images from time-lapse movies showing the progression of a cell rearrangement over time. optoGEF embryos showed increased numbers of newly formed edges oriented diagonally (not parallel) to the AP axis compared to controls (compare red arrows in images at right). optoGAP embryos showed increased times to resolve a vertex during cell rearrangement compared to control or optoGEF embryos.